EES Batteries

Accepted Manuscript

This article can be cited before page numbers have been issued, to do this please use: M. Woo and G. P. Demopoulos, *EES Batteries*, 2026, DOI: 10.1039/D6EB00077K.

View Article Online
DOI: 10.1039/D6EB00077K

Broader Context

The proliferation of autonomous systems and robotics requires next-generation batteries capable of delivering extreme energy density and rapid-charging kinetics. Lithium cobalt phosphate ($LiCoPO_4$, LCP) is uniquely positioned to meet these rigorous demands for niche applications as it shares the robust olivine framework yet offers a significantly higher operating voltage to surpass current energy limits. However, its commercial viability remains restricted by accelerated interfacial decay and severe chemical instability at the electrode-electrolyte boundary under high-voltage (high-V) operation.

To address these challenges, comprehensive post-mortem analyses were performed to elucidate interfacial degradation, leading to the application of interfacial coordination chemistry control via a functionalized carbon layer (FCL) coating. This versatile and scalable protocol stabilizes high-V cathodes through a synergistic defense mechanism that can be seamlessly integrated into various cathode production lines. By providing new insight and straightforward surface coating method, this work opens a rewarding pathway towards development of high-V cathodes for demanding energy storage applications.

View Article Online
DOI: 10.1039/D6EB00077K

ARTICLE

Insight and regulation of interfacial coordination chemistry of high-voltage $LiCoPO_4$ cathode via functionalized carbon layer anchoring for robust surface passivation

Received 00th January 20xx,
Accepted 00th January 20xx

DOI: 10.1039/x0xx00000x

Moohyun Woo [a] and George P. Demopoulos [a]*

Lithium cobalt phosphate ($LiCoPO_4$, LCP) is a high-voltage (high-V) polyanionic compound, of critical importance for high energy density. However, LCP's application has been hampered by inferior Coulombic efficiency and capacity retention owing to cathode degradation triggered by the elevated cut-off voltage of 5.0 V vs. Li/Li^+. Namely, such high-V leads to severe parasitic side reactions at the cathode-electrolyte interface involving complex phenomena, the understanding of which holds the key to designing robust high-V cathodes. Herein, post-mortem analysis of cycled LCP electrodes in different aging conditions revealed fundamental capacity fade mechanism at high-V interfaces. Detrimental degradation occurs through redox metal (RM) dissolution, caused by undesired electrochemical and chemical reactions with electrolyte. This process induces cation vacancies, leading to lattice collapse and progressive structural ingress. To combat this, we successfully engineered sucrose-derived functionalized carbon layer (FCL) anchoring strategy to regulate interfacial coordination chemistry. This conductive FCL layer serves a dual role: (i) expediting charge-transfer kinetics by establishing an efficient electronic network, and (ii) anchoring surface cations, thereby promoting a protective inorganic-enriched cathode-electrolyte interphase (CEI) layer characterized by Li-F and Co-F species while suppressing organic ligand-induced dissolution. This passivation suppresses structural ingress and preserves olivine structure, resulting in significantly enhanced rate capability and cycling stability.

Introduction

The rise of energy-intensive applications, ranging from grid-scale energy storage systems (ESS) to unmanned aerial vehicles (UAVs) and robotics, has driven the demand for next generation Li-ion batteries (LIBs) beyond the current energy density level.[1-4] To surpass these energy thresholds, it is essential to develop advanced cathode materials based on several selection criteria including operating voltage, storage capacity, rate capability, and cycling stability.[5-7] Design and development of high-voltage (high-V) cathodes is identified as a critical step in the pursuit for high energy density LIBs.[8] In the context, lithium cobalt phosphate ($LiCoPO_4$, LCP) is of great interest as a high-V polyanionic compound with high theoretical energy density of 800 Wh kg^{-1} thanks to the redox voltage and capacity (4.8 V × 167 mAh g^{-1}) properties.[9] Additionally, LCP, like its commercial counterpart lithium iron phosphate ($LiFePO_4$, LFP), belongs to the olivine crystal structure family, boasting a robust framework.[10,11] These attributes, despite its cobalt (Co) content, have made LCP a strong candidate for niche applications where high energy density systems are critical.[12,13]

Despite these promising benefits, the development of LCP cathodes has been hampered by certain compromising inherent material properties: (1) intrinsically low ionic and electronic conductivity causing sluggish kinetics, (2) abundant anti-site defects blocking one-dimensional (1-D) Li-ion diffusion pathway, and (3) capacity fade predominantly due to interphasial degradation at high-V—a relatively less explored yet critical contributor requiring further investigations.[14-16] Recently, we have developed a novel crystal variety of LCP characterized by shortened Li-ion diffusion length attributed to preferential crystal growth and defect-free structure.[17] This architecture, realized via solvent molecule-crystal plane regulation and subsequent argon (Ar)-annealing, enables the achievement of nearly theoretical full discharge capacity and remarkable rate capability. In spite of these significant bulk-level improvements, high-V interfacial instability stands as a critical bottleneck, where persistent capacity fade upon prolonged cycling indicates that electrolyte decomposition seemingly negates the protection offered by high-V stabilizing electrolyte additives. This observation implies that the capacity fade is not merely an acceleration of electrolyte decomposition, but rather a result of intricate and multifaceted interfacial side reactions that remain poorly understood. Accordingly, fundamental and comprehensive post-mortem investigations are required under various electrochemical environments with different aging/cycling conditions at the raised cut-off voltage, to provide insights as to the origin of LCP capacity fade. At the same time, research into surface engineering to mitigate destructive electrode-electrolyte interfacial reactions via proper functional surface coating is of great urgency to improve charge transport kinetics and prevent capacity fade via interface stabilization.

[a] Materials Engineering, McGill University, 3610 rue University, Montréal, QC H3A 0C5, Canada. Email: george.demopoulos@mcgill.ca

View Article Online
DOI: 10.1039/D6EB00077K

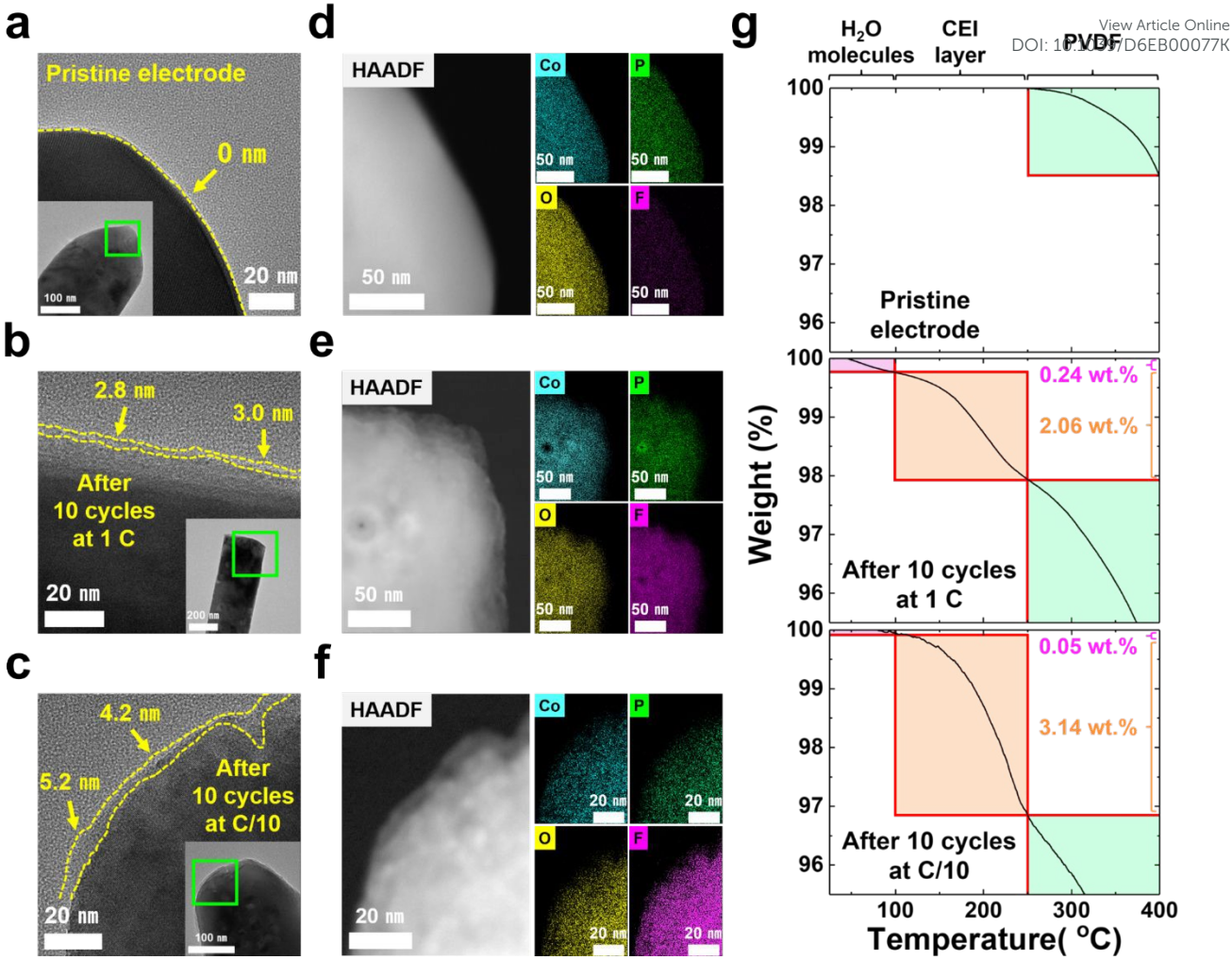

Fig. 1 (a-c) HRTEM images displaying CEI layer evolution from pristine state, to after 10 cycles at 1 C and C/10; (d-f) the corresponding HAADF and elemental mapping (Co, P, O, and F) images; and (g) the respective TGA curves up to 400 °C.

In this work, we scrutinized the correlation between capacity fade and irreversible interfacial reactions by conducting extensive post-mortem analysis. Our investigation reveals that the interfacial degradation of LCP proceeds through considerable redox metal (RM) dissolution under relatively long-term cycling operations. These side reactions lead to progressive lattice collapse and structural ingress into the particle interior. This degradation is primarily driven by chelating organic compounds as a result of electrolyte oxidation at the elevated voltage. These compounds coordinate with and extract LCP surface cations from olivine framework, leaving behind interfacial defects responsible for the observed capacity fade. To mitigate this, we developed a sucrose-derived functionalized carbon layer (FCL) anchoring strategy that provides multi-functional passivation through synergistic mechanisms. FCL substantially stabilizes the interface through a tailored coordination chemistry, beyond its intrinsic role of carbon layer in facilitating charge-transfer kinetics and serving as a physical barrier against direct electrolyte contact. Notably, oxygen-containing functional groups on FCL anchor surface cations via strong coordination, which actively promotes the formation of a robust inorganic-enriched cathode-electrolyte interphase (CEI) layer characterized by Li-F and Co-F species. This newly evolved interphase further reinforces the interfacial stability by effectively preventing the chelation by organic ligands. Consequently, our strategy demonstrates remarkable rate capability, achieving nearly theoretical Li-ion storage capacities across all C-rates, ranging from C/10 to 1 C. Remarkably, at 1 C rate, it delivers an outstanding discharge capacity of 163.0 mAh g^{-1} (equivalent to 771.2 Wh kg^{-1} in energy density) and relatively enhanced retention (76.36 % after 100 cycles).

Results and discussion

Irreversible interfacial aging of $LiCoPO_4$ upon cycling

Structural and compositional variation at the electrode-electrolyte interface was probed via post-mortem HRTEM, HAADF, and elemental mapping techniques and the obtained results are compiled in Fig. 1a-f. Pristine LCP prior to high-V operation (Fig. 1a) displays a smooth surface topography without any observable features of foreign precipitates. However, HRTEM images (Fig. 1b-c) reveal the formation of thicker CEI layer at the slower rate, C/10 compared to 1 C. This rate-dependency indicates that the prolonged high-V exposure upon charge-discharge process promotes further electrolyte

decomposition, leading to the remarkable CEI layer growth. Furthermore, HAADF and elemental mapping (Fig. 1d-f) demonstrate a stark contrast between pristine and cycled electrodes, as evidenced by gradual topographic roughening and foreign elemental deposition arising from these parasitic side reactions.[18-21] Pristine LCP (Fig. 1d) retains its intact surface topography, consistent with HRTEM result (Fig. 1a), while exhibiting only a trace amount of fluorine (F) due to PVDF binder, alongside the constituent elements of LCP including cobalt (Co), phosphorus (P), and oxygen (O). On the other hand, cycled LCP (Fig. 1e-f) shows pronounced topographic roughening and markedly elevated F concentration, both indicative of irreversible interfacial degradation as a result of side reactions with electrolyte. As this degradation progresses, parasitic ingress into LCP bulk crystals emerges, resulting in the graded zoning in the sub-surface region. This phenomenon could imply that RM dissolution (leaching) occurs concurrently with CEI layer evolution, as will be further elucidated in the following sections.

Thermogravimetric analysis (TGA) further substantiates topographic and compositional alterations, providing complementary validation of the mass evolution associated with the rate-dependent interfacial degradation. The weight loss for pristine and cycled electrodes (Fig. 1g and Fig. S1) can be categorized into four distinct temperature regimes, each attributed to the thermal response of specific components: i) Absorbed water (H_2O) evaporation (25-100 ^oC), which is negligible because of the storage in Ar-filled glovebox (< 0.5 ppm of H_2O and O_2); ii) CEI layer dissociation (100-250 ^oC); iii) PVDF binder decomposition (250-500 ^oC); and iv) Acetylene black combustion (above 500 ^oC).[22,23] After the heat treatment, the final mass remained is almost 70 wt.% accurately corresponding to the ratio of LCP active material in the electrode composition. To further investigate, TGA profile below 400 ^oC was analyzed in detail to assess CEI layer evolution upon electrochemical cycling. Considering the pristine electrode as a baseline, we can clearly see the weight loss involved with PVDF to occur above 250 ^oC. Yet, there is another discernible weight loss occurring in the temperature range, 100-250 ^oC for both cycled electrodes at 1 C (2.06 wt.%) and C/10 (3.14 wt.%) that must be assigned to the quantity of newly evolved CEI layer. The overall TGA results (Fig. S1c) also provide indirect evidence of RM dissolution (signaled by parasitic ingress shown in Fig. 1f) given that the mass of cycled LCP active material drops below 70 wt.% after the heat treatment. Typically, CEI layer consists of organic compounds and poorly crystalline materials with relatively low atomic weights. In contrast, dissolution of Co-containing species from Co-P-O framework would theoretically result in more significant mass loss due to the higher atomic weight of Co. This theoretical consideration supports interpreting the sub-70 wt.% final mass as an indirect indicator of Co dissolution, providing a reasonable scientific basis drawn from our obtained data. Accordingly, these findings underscore the urgent need for a surface functionalization strategy to passivate LCP interface and suppress irreversible RM dissolution.

One-step facile surface coating with functionalized carbon layer

To mitigate the irreversible side reactions at the interface, we introduced a surface coating strategy to protect LCP surface. For this purpose, different amounts of sucrose (30, 40, and 50 wt.%) were employed as a carbon source and dissolved in D.I. water, into which solvothermally-synthesized LCP (ST-LCP) powder was added and agitated. The coated LCP was obtained after drying and annealing in Ar atmosphere, following the same protocol established for solvothermally-synthesized and Ar-annealed LCP (referred to as ST-A-LCP).[17] In order to determine the optimal loading of sucrose, preliminary electrochemical evaluations (Fig. S2) were applied to LCP samples before and after coating. The sample with 40 wt.% of sucrose presents the most promising electrochemical results with respect to accessible initial discharge capacity at 1 C and retention after 100 cycles compared to the other concentrations. To assess the structural integrity, Rietveld refinement (Fig. S3 and Table S1) confirms that coated LCP sample retains its phase purity, with only a marginal increase in anti-site defect concentration relative to ST-A-LCP. Moreover, electron microscopy analysis (Fig. 2a-b) reveals that our coating process does not affect the anisotropically grown morphology for shortened Li-ion diffusion length, while HRTEM imaging displays a continuous and conformal carbonaceous shell of approximately 7-9 nm.[17]

Further spectroscopic techniques (Fig. 2c-f) including XPS, Raman, and FT-IR were carried out to verify the chemical nature of coated surface layer. In particular, XPS results show the presence of carbon (C 1s) and oxygen (O 1s). The C 1s spectra (Fig. 2c) were fitted with multiple carbon atom peaks corresponding to non-oxygenated and different oxygen-containing functional groups such as C=C, C-C, C-OH, C-O-C, C=O, COOH, and π-π interactions mediated by delocalized electrons in aromatic network.[24-27] In addition, the O 1s spectra (Fig. 2d) were deconvoluted into peaks corresponding to phosphate group (PO_4) and various functional groups such as C=O, COOH, C-OH, and C-O-C.[28,29] The specific binding energies, full width at half maximum (FWHM), and atomic percentage for these identified peaks are listed in Table S2. Collectively, XPS analysis confirms that the coating is predominantly carbonaceous, incorporating a high density of oxygen-containing functional groups. These chemical features imply the successful formation of functionalized carbon layer (FCL) as a uniform coating layer on LCP surface.

To validate these findings, Raman and FT-IR spectra were also collected. Raman spectrum (Fig. 2e) displays the combined vibration modes at lower and higher Raman shift. At lower shift region, three main vibrations were detected at 944, 1349, and 1593 cm^{-1} corresponding to PO_4, carbon D and G bands, respectively. The second-order bands centered at 2714, 2910, and 3151 cm^{-1} corresponding to 2D, D+G, and 2G peaks are attributed to overtone and combination of D and G bands. These spectral signatures are indicative of a disordered carbon structure commonly derived from the low-temperature pyrolysis of organic precursors, such as sucrose utilized in this study.[30,31] At the same time, FT-IR technique was also employed

View Article Online
DOI: 10.1039/D6EB00077K

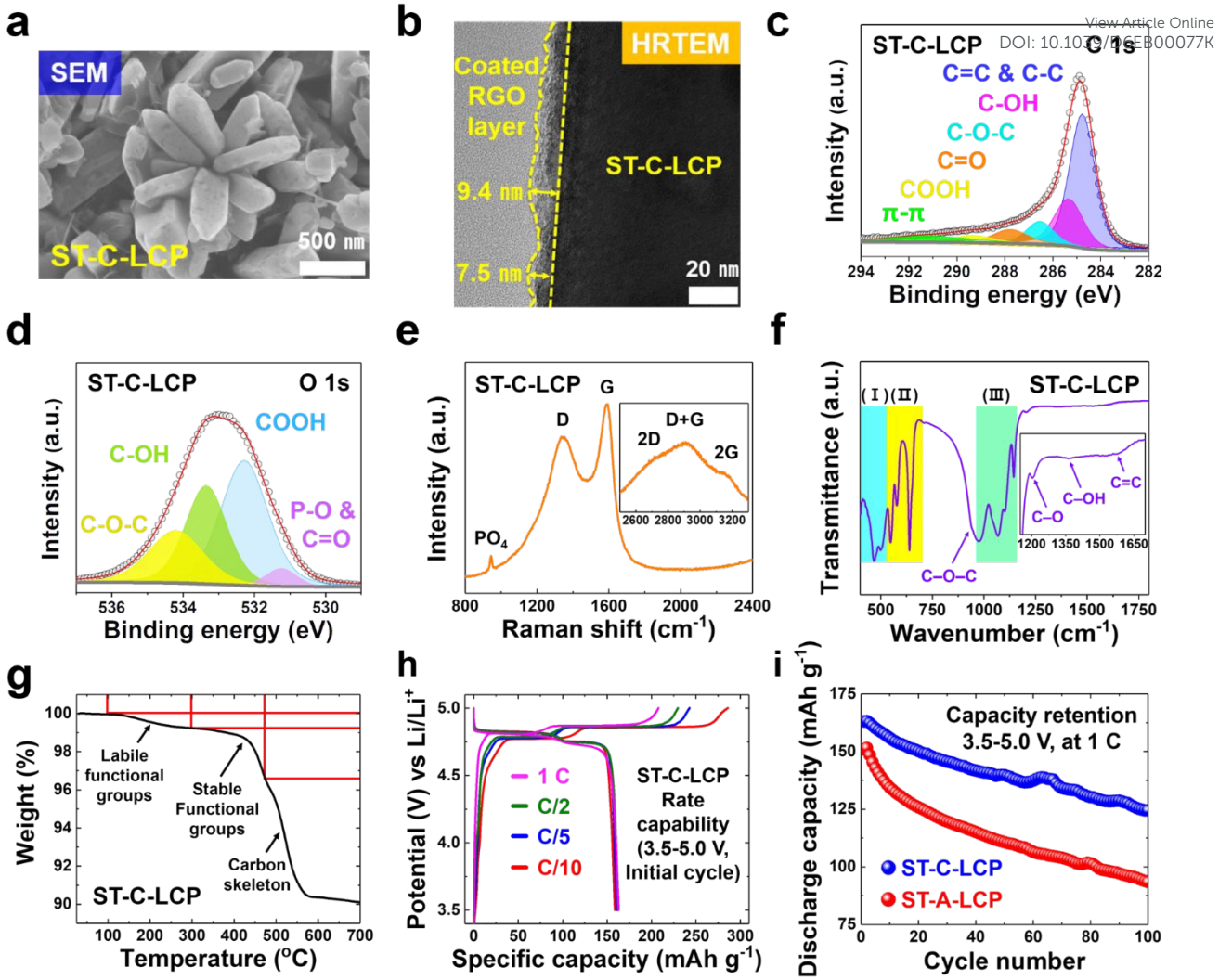

Fig. 2 Structural and electrochemical characterizations of FCL on ST-C-LCP surface: (a) SEM and (b) HRTEM images; XPS spectra of (c) C 1s and (d) O 1s; (e) Raman, (f) FT-IR, and (g) TGA profile confirming the presence of FCL and its functional groups; (h) rate capability at various C-rates from C/10 to 1 C; and (i) discharge capacity retention of ST-A-LCP and ST-C-LCP within the voltage range 3.5-5.0 V vs. Li/Li^+ at 1 C.

to prove the existence of FCL on LCP crystals. In principal, both LCP samples before (Fig. S4) and after coating (Fig. 2f) are mainly dominated with three stretching and vibration modes of (I) Li-ion (450-550 cm^{-1}) and (II & III) PO_4^{3-} group (500-700 and 900-1200 cm^{-1}).[32] However, we note that the coated sample exclusively incorporates extra features which are not strong but still persistent, originated from the stretching vibration of functional groups in FCL such as C-O-C (942 cm^{-1}), C-O (1205 cm^{-1}), C-OH (1363 cm^{-1}), and C=C (1580 cm^{-1}) unlike ST-A-LCP.[33,34] Accordingly, the coating is confirmed as FCL rich in oxygen-containing functional groups, successfully deposited via one-step facile low-temperature pyrolysis of sucrose, and the coated LCP sample is hereafter denoted as ST-C-LCP.

After the confirmation of FCL, we applied TGA analysis (Fig. 2g) to accurately quantify FCL derived from sucrose. The entire weight loss was recorded from room temperature to 700 °C with the ramping rate being 10 °C min^{-1} in air. Three distinct sections of weight loss were evidently observed at different temperature ranges: (i) Labile oxygen-containing functional group decomposition (100-300 °C, 0.76 wt.%), (ii) Stabilized oxygen-containing functional group removal (300-450 °C, 2.73 wt.%), and (iii) Carbon skeleton pyrolysis (450-700 °C, 6.41 wt.%).[35,36] On the other hand, TGA result of ST-A-LCP (Fig. S5) shows the whole mass preserved without any weight loss up to 700 °C. We note that, by simply utilizing 40 wt.% sucrose, FCL coating of almost 10 wt.% was yielded by the carbonization process during Ar-annealing, as in the case of ST-A-LCP preparation. Moreover, these functional groups facilitate uniform anchoring through strong coordination with LCP surface cations. These polar oxygen species promote rigid coordination interactions, ensuring a homogeneous interfacial coverage across the entire LCP crystals.[37-39] Concurrently, the intrinsic properties of FCL, specifically its large surface area and superior electronic conductivity, establish an expedited charge-transfer network.[40,41] This interfacial architecture is expected to work synergistically with the bulk-level improvements via ST synthesis, which enhances Li-ion diffusivity.

Reflecting these structural and interfacial modulations, ST-C-LCP demonstrated significantly improved electrochemical performance. Indeed, the exceptional rate capability (Fig. 2h) was observed, with discharge capacities of 158.8, 160.9, 162.6, and 163.0 mAh g^{-1} across all tested C-rates from C/10 to 1 C, which nearly approach the theoretical capacity. Thus, the anisotropically grown LCP crystals via ST synthesis can be

View Article Online
DOI: 10.1039/D6EB00077K

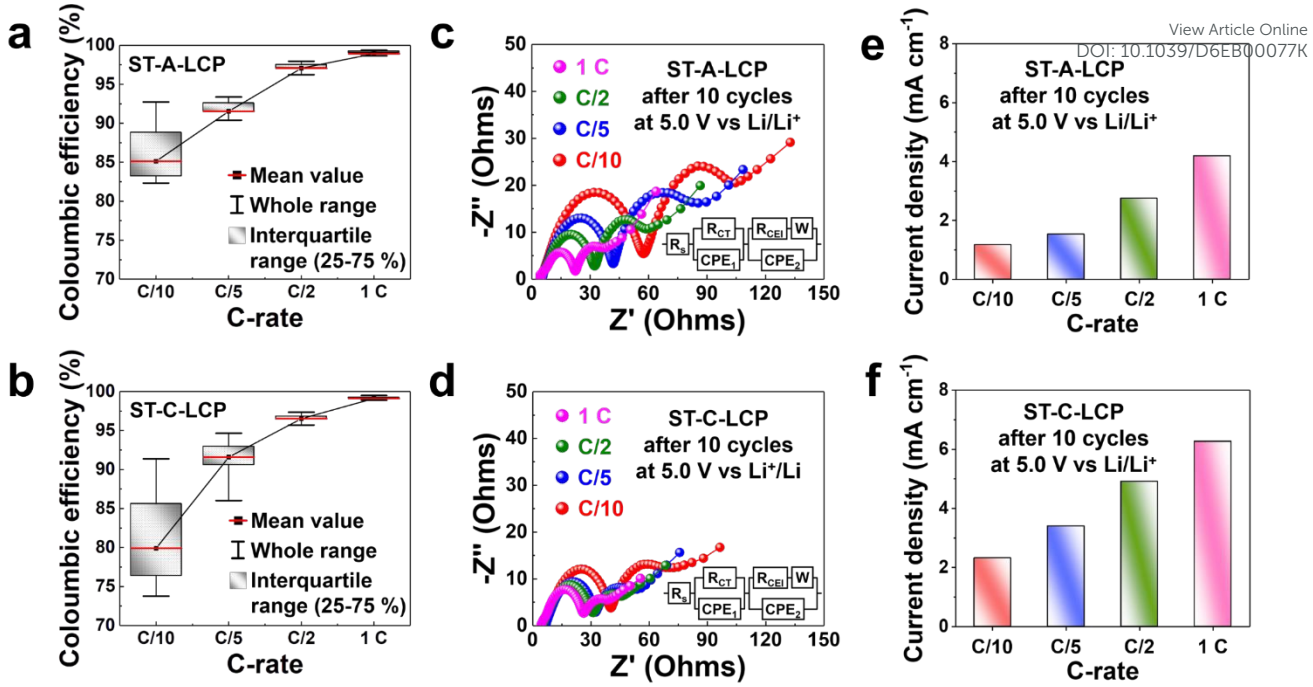

Fig. 3 Comparative post-mortem electrochemical analysis of ST-A-LCP and ST-C-LCP electrodes cycled at various C-rates: (a-b) Coulombic efficiency distribution as function of C-rate; (c-d) EIS analysis (the inset image shows the equivalent circuit model); (e-f) current density measurement from the Nyquist plot under the applied forward bias of 5.0 V vs. Li/Li^+.

effectively coated with conductive FCL successfully overcoming the sluggish kinetics by facilitating both Li-ion diffusion and electron transport. Beyond the rate capability, the long-term cycling stability (Fig. 2i) was boosted to 76.36 % compared to 61.65 % for ST-A-LCP during the initial 100 cycles at 1 C. The distinct gap in capacity retention (Fig. S6) is further highlighted by the comprehensive profile throughout the entire cycle periods for both LCP samples. Our proposed coating strategy enhances the cell durability as evident by the number of cycles enabled until the discharge capacity drops to 50 mAh g^{-1} (700 cycles for ST-C-LCP compared to 250 cycles for ST-A-LCP). Notably, ST-C-LCP exhibits improved capacity retention (Fig. S7) over prolonged cycling at relatively faster C-rates (C/5, C/2, and 1 C) with the sole exception of C/10.

Furthermore, to provide an objective and broader evaluation, a comparative plot has been introduced in Fig. S8, benchmarking the electrochemical performance of ST-C-LCP against previously reported carbon coating strategies on LCP systems. The plot correlates cycle number with final discharge capacity, with distinct symbols assigned to each C-rate to facilitates at-a-glance performance comparison. Notably, the data point corresponding to the present work is positioned toward the upper right region, demonstrating that our FCL delivers outstanding capacity retention compared to the existing literatures. To provide additional context for this comparison, the specific experimental parameters of each surveyed study, including carbon source, electrode-electrolyte composition, voltage ranges, and initial discharge capacity are summarized in Table S3.

Nevertheless, the role of FCL in modulating electrochemical environment and its subsequent impact on rate capability and capacity retention are not fully elucidated yet. Therefore, further investigations will be followed to uncover how FCL coating contributes to the enhancements of both charge-transfer kinetics and long-term cycling stability of ST-C-LCP.

Enhanced charge-transfer kinetics via FCL conductive network

To examine the impact of conductive FCL on charge-transfer kinetics, we initially investigated the statistical distribution of Coulombic efficiency (Fig. 3a-b) recorded over the number of cycles until the discharge capacity reached 50 mAh g^{-1}. This analysis encompasses entire distribution, mean value, and interquartile range, with the corresponding numerical data presented in Table S4 and S5. We note that both LCP electrodes exhibit their lowest average Coulombic efficiency and widest distribution spread at C/10. This is evidently due to the prolonged exposure of active material and electrolyte to high-V conditions at the slowest C-rate. Such extended residence time exacerbates an oxidative degradation at the interface, leading to considerable extra charge capacity.

Meanwhile, as C-rate increases, the average Coulombic efficiency gradually rises, and the statistical distribution significantly narrows. In this regard, the observed trends corroborate the rate-dependent nature of irreversible side reactions, which can be interpreted as a function of high-V exposure duration. To clearly demonstrate the rate-dependent cycling stability, we compared the average Coulombic efficiency at two distinct conditions: C/10 and 1 C. At the slowest rate (C/10), ST-C-LCP features the diminished average Coulombic efficiency (79.90 % vs. 85.12 % for ST-A-LCP). This finding indicates that electrons generated from oxidative decomposition at high-V are more readily transported to LCP electrode due to superior electronic conductivity and enlarged active surface area of FCL resulting in undesired extra charge currents.[40,41] In other words, FCL serves as a “double-edged sword” as it does improve rate capability, but cause severe

View Article Online
DOI: 10.1039/D6EB00077K

degradation at slower C-rates, which in turn leads to inferior and unevenly distributed Coulombic efficiency. However, this drawback is largely mitigated at 1 C. Under this condition, ST-C-LCP delivers the enhanced average Coulombic efficiency (99.10 % vs. 98.57 % for ST-A-LCP) by effectively curtailing high-V exposure time due to accelerated charge-transfer kinetics. Indeed, as shown in Fig. S9, Coulombic efficiency of both LCP electrodes exhibits comparable values at 1 C, indicating that conductive FCL does not contribute to any significant extra charge capacity at higher rates.

Post-mortem EIS analysis was subsequently performed to substantiate these kinetic advantages. Nyquist plots (Fig. 3c-d) were obtained under the applied forward bias of 5.0 V vs. Li/Li^+ for cycled cells, a condition that simulates the delithiation process and captures the resistance encountered as Li-ions migrate from LCP lattice toward electrolyte. For all EIS patterns, two semi-circles were observed in high- and mid-frequency regions, in addition to a long tail at low frequency. The formation of CEI layer during cycling establishes a complex LCP-CEI-Electrolyte structure, effectively creating two distinct interfaces. Accordingly, two semi-circles are assigned to the resistance associated with LCP-CEI and CEI-Electrolyte interfaces, respectively. In this model, the first semi-circle in the high-frequency region represents the charge-transfer resistance (R_{CT}) at LCP-CEI interface, where Li-ions are extracted from LCP lattice. In parallel, the second semi-circle, appearing in the mid-frequency range, corresponds to the resistance (R_{CEI}) at CEI-Electrolyte interface, reflecting the barrier for Li-ions to penetrate the evolved CEI layer and enter the liquid phase. The expansion in the diameters of both semi-circles is attributed to the increased thickness and density of CEI layer formed under high-V conditions, which hampers efficient Li-ion transport.[42] Notably, both LCP electrodes display enlarged semi-circle diameters at slower C-rates, reflecting a thicker CEI layer due to prolonged high-V exposure that progressively impedes Li-ion intercalation. However, ST-C-LCP demonstrates markedly smaller diameters of high-frequency (R_{CT}) and mid-frequency (R_{CEI}) semi-circles across all C-rates. This significant reduction in resistance confirms that FCL coating effectively mitigates excessive CEI layer growth by expediting charge-transfer kinetics, thereby minimizing the residence time at high-V. These findings are in excellent agreement with the narrower Coulombic efficiency distribution observed at 1 C, collectively highlighting the role of FCL in maintaining a stable and thin interfacial architecture.

Moreover, the kinetic implications of the evolving CEI layer are quantitatively evaluated through the current density (Fig. 3e-f) derived from Nyquist plots. These measurements, conducted under the applied forward bias of 5.0 V vs. Li/Li^+, further validate the rate-dependent resistance trend discussed above. ST-A-LCP exhibits a significant decline as C-rate is reduced, yielding values of 4.19, 2.75, 1.53, and 1.17 mA cm^{-1} at 1 C, C/2, C/5 and C/10, respectively. In contrast, ST-C-LCP demonstrates a substantial boost in current density across all C-rates, with values increasing by 6.27, 4.91, 3.40, and 2.32 relative to ST-A-LCP at corresponding rates. In addition, ST-C-LCP showed a shortened current density decay period (Fig. S10 and S11) of 200 seconds, compared to 400 seconds observed for ST-A-LCP. These results underscore the intimate correlation between C-rate and progressive CEI evolution. Indeed, slower rates extend the timeframe of high-V exposure, which facilitates thicker CEI formation and subsequently suppresses the current response.

By mitigating this effect, we have demonstrated that FCL network plays a critical role in accelerating charge-transfer kinetics, thereby providing a fundamental basis for the enhanced rate capability of LCP. This improvement not only paves a way for LCP in niche sectors requiring high power density but also establishes a fundamental design principle for high-V cathode systems. Specifically, minimizing high-V exposure duration through the expedited kinetics can serve as an effective strategy for preserving interfacial integrity, as CEI layer evolution remains inevitable despite incorporating the high-V stabilizing electrolyte additive. Building upon the observed kinetic advantages of FCL coating, the next section further scrutinizes the chemical composition of CEI layer through XPS analysis to identify the origin of improved long-term cycling stability.

Inorganic-enriched CEI formation via FCL anchoring effect

The correlation between CEI layer composition and prolonged cycle life was probed through post-mortem XPS analysis, as compiled in Fig. 4. All corresponding values, including binding energy, FWHM, and atomic percentage of each peak are listed in Table S6-9. This investigation compared the pristine electrode as a baseline with cycled electrodes that had reached a discharge capacity at 50 mAh g^{-1} at rates of C/10 and 1 C. This comprehensive dataset focuses on three relevant elements of CEI layer composition (C 1s, O 1s, and F 1s) to track the chemical evolution of interface across two different cycling regimes.

Regarding C1 spectra (Fig. 4a-b) of pristine electrodes, multiple peaks are observed at characteristic binding energies for C-C, C-H, C-O, C=O and O-C=O, originating from the conductive acetylene black.[43] In addition, C-F and CH_2-CF_2 peaks are attributed to PVDF binder, which is another essential electrode component.[44] In the pristine state, ST-C-LCP possesses higher atomic percentages of carbon skeleton (C-C) and oxygen-containing functional groups (C=O and O-C=O) than those of ST-A-LCP (Table S6 and S7). This enrichment is directly attributed to FCL successfully coated on LCP crystals, establishing the integrated conductive carbonaceous network. After cycling at 1 C, both electrodes exhibit a relative enhancement in the intensity of most peaks in C 1s spectra, with the exception of C-C peak (Table S8 and S9). This trend corroborates progressive CEI layer formation arising from the oxidative decomposition of carbonate solvents (EC, PC, and DMC) and $LiPF_6$ salt in electrolyte, accelerated by high-V operation.[45,46] Notably, CH_2-CF_2 peak in cycled ST-C-LCP increases sharply from 9.79 to 19.07 %, whereas ST-A-LCP displays only a marginal rise from 12.54 to 15.90 %. This observation implies that FCL might facilitate the enrichment of fluorinated species at the interface. This compositional shift is further substantiated by F 1s analysis discussed below.

View Article Online
DOI: 10.1039/D6EB00077K

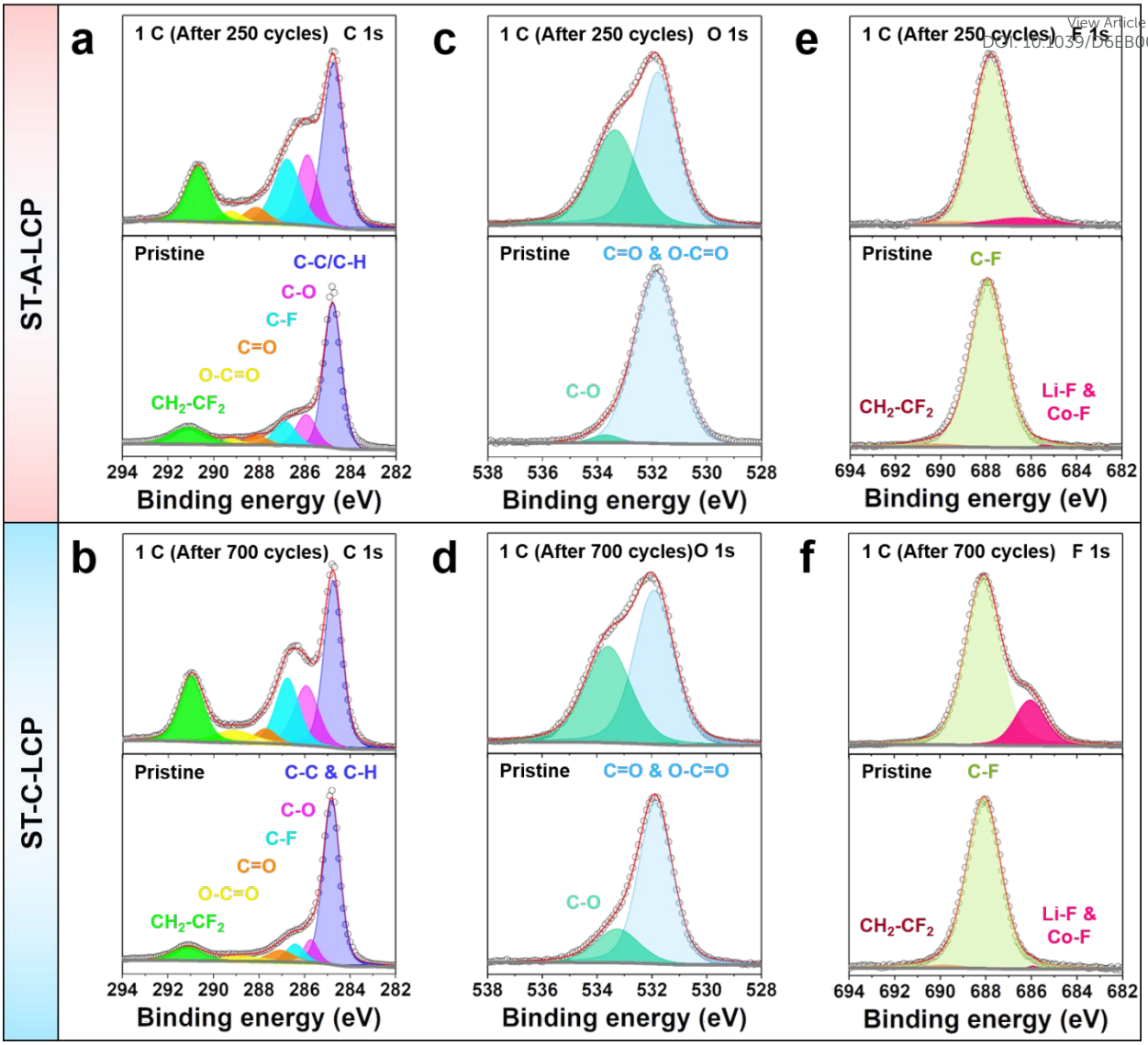

Fig. 4 High-resolution XPS spectra of (a-b) C 1s, (c-d) O 1s, and (e-f) F 1s for pristine and cycled ST-A-LCP and ST-C-LCP electrodes, illustrating the chemical evolution of CEI layer after 250 and 700 cycles at 1 C, respectively.

Likewise, O 1s spectra (Fig. 4c-d) reveal distinct compositional changes between pristine and cycled electrodes for both LCP samples. In the pristine state, ST-C-LCP shows a relatively higher concentration of oxygen-containing functional groups, such as C-O, owing to the integrated FCL coating. We note that upon cycling, C-O peak intensity becomes remarkably dominant, surging from 3.95 to 42.03 % for ST-A-LCP and from 21.26 to 42.08 % for ST-C-LCP (Table S8 and S9). This dramatic chemical shift is intimately related to the oxidative decomposition of carbonate solvents at high-V.

To elucidate the precise driving force behind this high-V degradation, the environmental constraints of cell assembly must be considered. While conventional models for RM dissolution presuppose the presence of trace H_2O and O_2 as prerequisites for acid-driven (e.g. hydrogen fluoride, HF) etching, the cell assembly in this study was strictly performed under an anhydrous and anaerobic environment with the moisture and oxygen levels maintained below 0.5 ppm. This stringent control effectively precludes such moisture-dependent pathways as the primary initiation mechanism for early-stage degradation. Under these environments, the oxidative decomposition of electrolyte solvents becomes the dominant factor at potentials above 4.5 V. In detail, cyclic carbonates (EC and PC) and their linear counterpart (DMC) undergo ring-opening and C-O bond cleavage, respectively, resulting in polymerization that evolves into β-diketonate-type ligands.[47] The coordination of these ligands with surface RM (Co) cations facilitates interfacial leaching by forming soluble metal-organic complexes. Such coordination involves electron transfer that reduces the oxidation state of Co. This process can be significantly promoted by the chemical instability of the fully delithiated $CoPO_4$ phase.[16,48] Specifically, the trivalent Co is prone to reduction back to the relatively stable divalent state through irreversible side reactions with electrolyte. The resulting redox tendency might provide an extra thermodynamic driving force to enhance interfacial coordination and subsequent Co dissolution. Consequently, this dissolution process triggers vacancy-induced lattice collapse

View Article Online
DOI: 10.1039/D6EB00077K

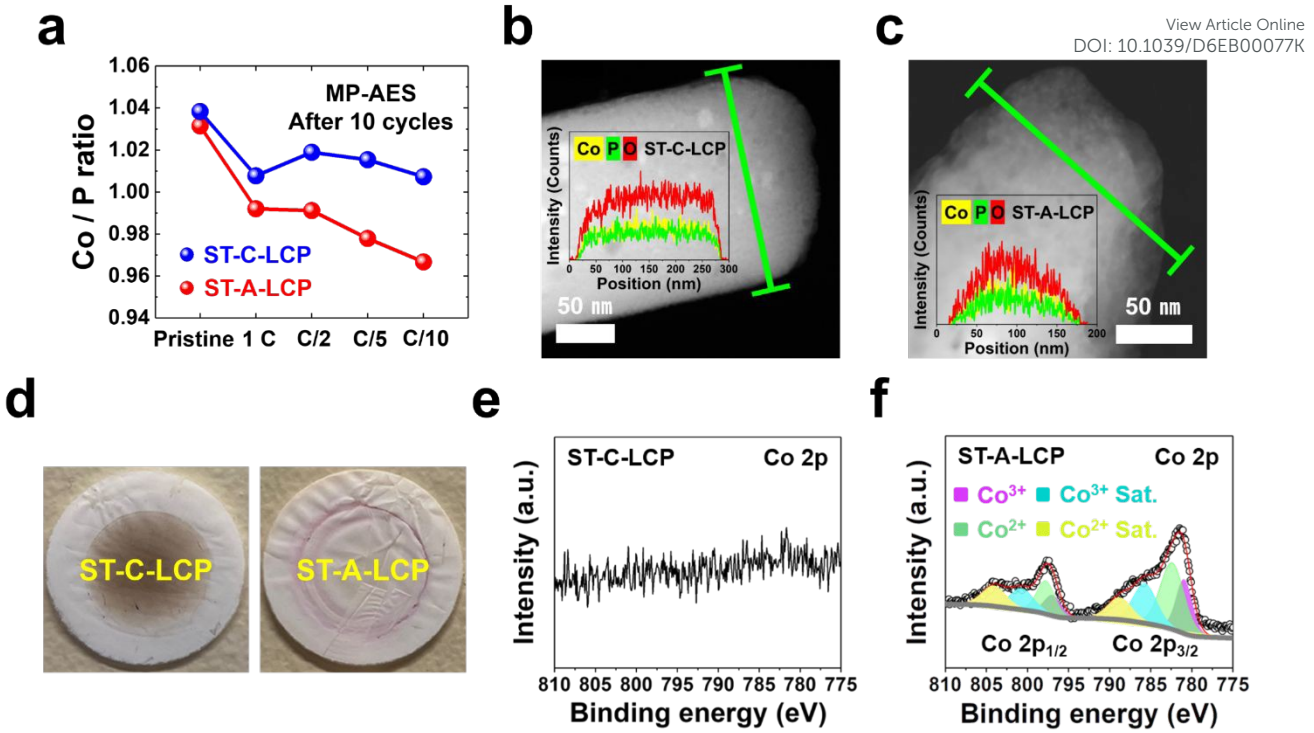

Fig. 5 Evaluation of RM dissolution and parasitic ingress on ST-A-LCP and ST-C-LCP upon cycling: (a) Co/P ratios of cycled electrodes after 10 cycles at various C-rates, determined via MP-AES; (b-c) HAADF images and line scans of cycled LCP particles after 100 cycles at 1 C; (d) photographs and (e-f) corresponding Co 2p XPS spectra of separators retrieved after 100 cycles at 1 C.

and structural ingress into the bulk. Thereafter, the soluble metal-organic complexes migrate to and accumulate within separator and anode, where they undergo electrochemical reduction and deposition during discharge process. This dissolution and migration mechanism fundamentally drives interfacial degradation leading to RM-related capacity loss. Furthermore, this complexation liberates H_2O as a byproduct.[47] The produced moisture further reacts with $LiPF_6$ salt to yield corrosive HF, which exacerbates the collapse of Co-P-O framework.[49,50] Hence, following this initial coordination-friven dissolution, the synergy between RM dissolution and HF attack establishes a comprehensive interfacial capacity fade mechanism for high-V cathode systems that compromises overall cell performance.

Unlike the aforementioned elements (C 1s and O 1s), F 1s spectra demonstrate a stark contrast between ST-A-LCP and ST-C-LCP. In the pristine state, both electrodes exhibit nearly identical features, predominantly characterized with C-F peak originating from PVDF binder. However, distinct CEI layer evolution pathways are observed upon cycling to the same degraded state at a discharge capacity of 50 mAh g^{-1}. Quantitatively, the atomic percentage of inorganic Li-F and Co-F species in cycled ST-A-LCP electrode marginally increases from 0.65 to 3.82 %, whereas ST-C-LCP exhibits a substantial rise from 0.4 to 18.94 %. This remarkable inorganic enrichment in ST-C-LCP, versus the organic-rich CEI layer in ST-A-LCP, is a direct consequence of the interfacial coordination chemistry engineering enabled by FCL anchoring. The oxygen-containing functional groups in FCL, possessing partially negative charges, effectively stabilize the LCP surface cations and facilitate the formation of inorganic-enriched CEI layer.[51-53] In turn, this coordination mechanism performs two critical functions: (i) ensuring uniform FCL coverage during fabrication, and (ii) modulating interfacial chemistry throughout electrochemical operation. By anchoring LCP surface cations, this FCL-mediated interface regulation promotes the formation of stable inorganic-enriched CEI layer. Building upon our observations, it is postulated that the resulting CEI layer ensures a robust passivation effect, which is likely responsible for the markedly enhanced capacity retention.

Moreover, it should be emphasized that previous research on LCP capacity fade has been largely confined to bulk structural issues and electrochemical side reactions, such as anti-site defect and CEI layer evolution.[54-58] However, chemical leaching at the electrode-electrolyte interface remains underexplored despite its significance, as evidenced by the crystal ingress phenomenon observed in this study (Fig. 1c and 1f). To address this knowledge gap, the following section further demonstrates how effectively this passivation suppresses interfacial degradation.

Interfacial passivation by FCL against RM dissolution and parasitic ingress

To verify the correlation between robust passivation and interfacial stability, Co/P molar ratios (Fig. 5a) were quantified via MP-AES technique for both LCP electrodes after 10 cycles at various C-rates. Pristine electrodes possess near-the stoichiometric Co/P ratio, with marginally 3 and 4 % of excess Co for ST-A-LCP and ST-C-LCP respectively. Relative to these values as a baseline, it is evident that Co/P ratio of ST-C-LCP remains well-preserved across all C-rates. In contrast, ST-A-LCP exhibits a noticeable reduction as C-rates decreases. As discussed in the previous sections, a slower C-rate leads to

prolonged exposure to high-V conditions, which facilitates Co dissolution through metal-organic complexation. Thus, the observed decline in Co/P ratio of ST-A-LCP at slower C-rates is attributed to this complexation-driven leaching, whereas the inorganic-enriched CEI layer in ST-C-LCP effectively suppresses this interfacial degradation.

To probe further this phenomenon, we employed TEM techniques including HRTEM, HAADF, and line scanning to examine LCP particles retrieved from electrodes after 100 cycles at 1 C. HAADF and HRTEM images (Fig. 5b and S12a) confirm the topographical integrity of ST-C-LCP without parasitic ingress owing to the robust passivation provided by FCL-mediated interface. Notably, the inset line scan image in Fig. 5b reveals the uniform elemental distributions of Co, P, and O in ST-C-LCP with the rectangular shape. On the other hand, we observed that ST-A-LCP crystal (Fig. 5c and S12b) exhibits pronounced "corrosion" signs and metal depletion, characterized by parasitic ingress that originates at the interface and gradually progressed toward LCP bulk structure. These results provide clear evidence that FCL coating largely prevents RM dissolution. In addition, these findings underline our postulation that RM dissolution occurring at the interface can be an important contributor to LCP capacity loss rather than alone the CEI layer inducing charge-transfer resistance.

To elucidate the unique passivation chemistry, extra post-mortem studies were undertaken focusing on the separators retrieved from cycled cells after 100 cycles at 1 C. The separators (Fig. 5d) collected from cycled ST-C-LCP and ST-A-LCP cells show an obvious optical difference. In particular, the separator from ST-A-LCP cell is seen to have a pinkish coloration apparently due to migration and deposition on it of dissolved Co species. To further substantiate, we probed the surface of separators via XPS characterization. XPS spectra (Fig. 5e-f) clearly present the particular bonding associated with Co detected solely in the separator that was cycled with ST-A-LCP electrodes. Meanwhile, no signal for RM dissolution is identified in ST-C-LCP even after undergoing the same number of charge-discharge cycles. Furthermore, the separator from ST-A-LCP cells reveals two different oxidation states of Co (Co^{2+} and Co^{3+}) simultaneously. Following the deconvolution of Co 2p spectrum (Co $2p_{3/2}$ and Co $2p_{1/2}$), the relative atomic ratio of Co^{2+} and Co^{3+} (Table S10) were determined to be approximately 64.6 and 35.4 %, respectively. We note that this value closely corresponds to the intermediate phase, $Li_{2/3}Co^{2+}{}_{2/3}Co^{3+}{}_{1/3}PO_4$ formed during Li-ion intercalation process.[59-61] This is consistent with the shrinking core model of LCP, where the intermediate phase persists at the electrode-electrolyte interface for the longest duration upon (de)intercalation.[59] Consequently, this intermediate phase serves as the primary source of the dissolved species with mixed oxidation states of Co detected in the separator. These findings clearly prove that parasitic ingress on the particle surface is the result of RM dissolution when LCP is exposed to high-V upon electrochemical cycling regardless of charge and discharge steps, since the redox reactions of RM ($Co^{2+}\leftrightarrow Co^{3+}$) initiate at the interface at high-V.[62-64] In contrast, FCL anchoring facilitates the formation of an inorganic-enriched CEI layer, which acts as a robust physical and chemical barrier. This passivation layer mitigates the complexation-driven leaching of RM cations, thereby maintaining the structural and compositional integrity of LCP surface.

Conclusion

In this work, we performed systematic post-mortem analysis of LCP cathodes to elucidate the interphasial degradation mechanism and advance an interfacial coordination chemistry engineering strategy via FCL anchoring to mitigate the resulting detrimental effects. Our findings revealed that high-V operation triggers RM dissolution from olivine lattice, serving as another critical contributor to capacity fade distinct from conventional anti-site defect and CEI evolution. Notably, this degradation is governed by the total high-V exposure duration upon cycling, which necessitates enhanced rate capability to mitigate such interfacial damages. These insights motivated us to develop the sucrose-derived FCL anchoring strategy. This approach aims to facilitate expedited charge exchange and regulate interfacial coordination chemistry, thereby markedly suppressing the undesirable side reactions at the interface. Specifically, oxygen-containing functional groups anchor surface cations, promoting the formation of a protective inorganic-enriched CEI layer predominantly composed of Li-F and Co-F that effectively inhibits RM dissolution. Consequently, this multi-functional interface enables outstanding rate capability (163.0 mAh g^{-1} at 1 C) with significantly enhanced retention (76.36 % after 100 cycles). The integration of preferential crystal engineering and FCL-mediated interfacial stabilization establishes practical design principles for high-V polyanionic cathodes. Furthermore, these optimized, defect-free LCP crystals can be subsequently enhanced through tailored doping scenarios and integration with solid-state electrolytes to achieve superior cycling stability even at 5.0 V (vs. Li/Li^+) operation. Ultimately, this work establishes a practical high-V cathode model and paves the way for high energy density LCP systems with extended cycle life.

Experimental section

Materials preparation

LCP materials were synthesized via a solvothermal (ST) process utilizing ethylene glycol (EG) as a reaction medium at 260 °C for 6-hour duration with agitation at 300 rpm. The precursor solution was prepared with a specific molar ratio of $Li:Co:PO_4$ = 2:1:1, while the concentration of Co and PO_4 source were maintained at 0.4 M. The comprehensive details regarding the chemicals and synthetic procedures are documented in our previous reports.[17,32] This methodology specifically designed to facilitate the preferential anisotropic crystal growth. For sucrose-derived functionalized carbon layer (FCL) coating, the method involved dispersion and stirring of pristine ST-LCP in deoxygenated deionized water containing sucrose (99.5 %, $C_{12}H_{22}O_{11}$, Sigma-Aldrich) of different weight percent (0, 30, 40, 50 wt.%). The well-mixed suspension was transferred in an alumina crucible. The slurry was then dried in a vacuum oven at 80 °C and transferred to an MTI mini tube furnace (model OTF-1200X) and heated at 700 °C for 1 hour with a continuous Ar gas flow to induce sucrose decomposition and subsequent

carbonization. The samples after Ar-annealing are denoted as 'ST-A-LCP' (without sucrose) and 'ST-C-LCP' (with sucrose).

Materials characterization

High-resolution transmission electron microscopy (HRTEM) with high-angle annular dark-field (HAADF) imaging and energy dispersive X-ray (EDS) analysis for elemental mapping was applied to monitor the evolved CEI and FCL using Thermo Scientific Talos F200X G2 STEM with the accelerating voltage of 200 kV. The morphology of LCP samples was evaluated with Hitachi cold-field emission SU-8000 scanning electron microscope (CFE-SEM). Thermogravimetic analysis (TGA) was performed in air from room temperature to 700 °C with the heating rate at 10 °C min^{-1} using TGA 5500 thermal analyzer and platinum crucibles for quantitative analysis of CEI and FCL. For the surface layer composition analysis, X-ray photoelectron spectroscopy (XPS) measurements were made with Thermo Scientific K-Alpha using aluminum (Al) Kα micro-focused monochromator. XPS data processing was performed with Avantage data system for peak fitting. Powder X-ray diffraction (PXRD) patterns were collected with Bruker D8 Discovery X-ray diffractometer using Co Kα radiation with the wavelength (λ) of 1.78892 Å from 2ϑ = 10 to 80 °. Crystal structure information for lattice parameters and anti-site defect concentration was fitted and estimated with XRD Rietveld refinement by using TOPAS Academic V5 software. The microwave plasma atomic emission spectrometer (MP-AES) from Agilent was used to determine the concentration ratio of remaining cobalt to phosphate (Co/P) in LCP retrieved from cycled electrodes. Prior to MP-AES measurements, cycled electrodes were soaked in ethanol and sonicated for 3 hours to separate LCP active material from acetylene black and PVDF binder. Subsequently, they were digested by using 50 vol.% concentrated hydrochloric acid (HCl, Fisher Scientific) followed by dilution with 4 vol.% nitric acid (TraceMetal Grade, HNO_3, Fisher Scientific). Raman spectroscopy (DXR2 Raman Microscope, Thermo Scientific) with 532 nm wavelength and Fourier transform infrared (FT-IR) spectroscopy (Perkin Elmer Spectrum II FT-IR Spectrometer) were employed in the wavenumber range of 4000 to 400 cm^{-1} with a resolution of 0.5 cm^{-1} to confirm the existence of FCL and its oxygen-containing functional groups on the surface of ST-C-LCP sample.

Battery assembly and electrochemical protocols

To fabricate the cathode electrode slurry, the active material (ST-A-LCP and ST-C-LCP), conductive acetylene black (Alfa Aesar), and polyvinylidene fluoride (PVDF, $(C_2H_2F_2)_n$, Sigma-Aldrich) binder were mixed in N-Methyl-2-Pyrrolidone (NMP, 99.5% C_5H_9NO, Sigma-Aldrich) solvent with a weight ratio of 7:2:1, corresponding to 140 mg, 40 mg, and 20 mg respectively. The slurry was pasted on a high-purity Al foil current collector and then dried overnight at 80 °C in a vacuum oven. The cathode electrodes were prepared with a diameter of 1 cm and a thickness of 0.3 mm, achieving an average mass loading of 2-2.5 mg cm^{-2}. Lithium (Li) metal (MSE Supplies) and polypropylene film (Celgard 2200) were used as anodes and separators. The customized electrolyte solution was prepared by dissolving 1 M of lithium hexafluorophosphate (> 97 % $LiPF_6$, TCI Chemicals) solution in a 1:1:3 (vol.%) mixture of ethylene carbonate (EC, 99 % $(CH_2O)_2CO$, Sigma-Aldrich), propylene carbonate (PC, 99.7 % $CH_3C_2H_3O_2CO$, Sigma-Aldrich), and dimethyl carbonate (DMC, 99 % $H_3COCOOCH_3$, Sigma-Aldrich) carbonate solvents, incorporating 2 wt.% tris(trimethylsilyl) phosphite (95 % $[(CH_3)_3SiO]_3P$, Sigma-Aldrich) as high-V stabilizing additive. The galvanostatic charge-discharge profile was measured on an Arbin cycler at an ambient temperature of 25 °C. The battery cycling test was carried out at different C-rates (1 C = 167 mAh g^{-1}) in the voltage range of 3.5-5.0 V vs. Li/Li^+. For capacity retention, we continued the cycling tests until the discharge capacity declined to 50 mAh g^{-1}. Electrochemical impedance spectroscopy (EIS) measurements of the pristine and cycled electrodes were made using a BioLogic workstation in potentiostatic mode between 1 MHz and 10 mHz with the forward bias potentials (5.0 V vs. Li/Li^+). Nyquist plots were fitted using ZView® software. The electrochemical data presented in this work corresponds to the representative cell performance that closely matches the median values of capacity and retention.

Post-mortem analysis

After performing the above-described electrochemical tests, cycled electrodes and separators were harvested in an Ar-filled glovebox (H_2O and O_2 < 0.5 ppm) and rinsed with DMC three times to remove residual electrolyte and Li salt. Subsequently, the collected electrodes and separators were dried in the glovebox for 48 hours. Further characterizations for crystal structure, surface, and elemental composition were carried out with the same protocols outlined above.

Author contributions

M. Woo performed all the experiments and characterizations with the interpretation of the results. G. P. Demopoulos supervised all aspects of the research.

Conflicts of interest

There are no conflicts to declare.

Data availability

The data that supports the findings of this study have been included as part of the supplementary information (SI). SI is available. See DOI: http://. Further information is available from the corresponding author upon reasonable request.

Acknowledgements

This research project funded by Natural Sciences & Engineering Research Council of Canada [NSERC Strategic Project Grant Number: NSERC STPGP 521217-18] was sponsored by Hydro-Québec's Centre of Excellence on Transportation Electrification and Energy Storage. Additional support via the McGill Engineering Doctoral Award program is gratefully acknowledged.

References

1 Z. Zhu, T. Jiang, M. Ali, Y. Meng, Y. Jin, Y. Cui and W. Chen, *Chem. Rev.*, 2022, **122**, 16610-16751.
2 V. Viswanathan, A. H. Epstein, Y.-M. Chiang, E. Takeuchi, M. Bradley, J. Langford and M. Winter, *Nature*, 2022, **601**, 519-525.
3 M. Dixit, A. Bisht, R. Essehli, R. Amin, C.-B. M. Kweon and I. Belharouak, *ACS Energy Lett.*, 2024, **9**, 934-940.
4 D. McNulty, A. Hennessy, M. Li, E. Armstrong and K. M. Ryan, *J. Power Sources*, 2022, **545**, 231943.
5 C. Liu, Z. G. Neale and G. Cao, *Mater. Today*, 2016, **19**, 109-123.
6 A. Konarov, S.-T. Myung and Y.-K. Sun, *ACS Energy Lett.*, 2017, **2**, 703-708.
7 A. M. Nolan, Y. Liu and Y. Mo, *ACS Energy Lett.*, 2019, **4**, 2444-2451.
8 W. Li, B. Song and A. Manthiram, *Chem. Soc. Rev.*, 2017, **46**, 3006-3059.
9 A. K. Padhi, K. S. Nanjundaswamy and J. B. Goodenough, *J. Electrochem. Soc.*, 1997, **144**, 1188.
10 C. Masquelier and L. Croguennec, *Chem. Rev.*, 2013, **113**, 6552-6591.
11 Y.-M. Kang, Y.-I. Kim, M.-W. Oh, R.-Z. Yin, Y. Lee, D.-W. Han, H.-S. Kwon, J. H. Kim and G. Ramanath, *Energy Environ. Sci.*, 2011, **4**, 4978-4983.
12 D. Liu, W. Zhu, C. Kim, M. Cho, A. Guerfi, S. A. Delp, J. L. Allen, T. R. Jow and K. Zaghib, *J. Power Sources*, 2018, **388**, 52-56.
13 J. Wu and C.-J. Tsai, *ACS Appl. Energy Mater.*, 2021, **4**, 6408-6413.
14 Y. Maeyoshi, S. Miyamoto, Y. Noda, H. Munakata and K. Kanamura, *J. Power Sources*, 2017, **337**, 92-99.
15 X. Wu, M. Meledina, J. Barthel, Z. Liu, H. Tempel, H. Kungl, J. Mayer and R.-A. Eichel, *Energy Storage Mater.*, 2019, **22**, 138-146.
16 J. G. Lapping, S. A. Delp, J. L. Allen, J. L. Allen, J. W. Freeland, M. D. Johannes, L. Hu, D. T. Tran, T. R. Jow and J. Cabana, *Chem. Mat.*, 2018, **30**, 1898-1906.
17 M. Woo, S.-W. Park, J. Lee, D.-H. Seo and G. P. Demopoulos, *Adv. Energy Mater.*, 2025, **15**, 2404404.
18 M. Woo, J. Lee and G. P. Demopoulos, *Mater. Adv.*, 2023, **4**, 4823-4834.
19 A. Tornheim, S. Sharifi-Asl, J. C. Garcia, J. Bareño, H. Iddir, R. Shahbazian-Yassar and Z. Zhang, *Nano Energy*, 2019, **55**, 216-225.
20 N. R. Park, Y. Li, W. Yao, M. Zhang, B. Han, C. Mejia, B. Sayahpour, R. Shimizu, B. Bhamwala, B. Dang, S. Kumakura, W. Li and Y. S. Meng, *Adv. Funct. Mater.*, 2023, **34**, 2312091.
21 M. Uitz, M. Sternad, S. Breuer, C. Täubert, T. Traußnig, V. Hennige, I. Hanzu and M. Wilkening, *J. Electrochem. Soc.*, 2017, **164**, A3503.
22 W. M. Dose, W. Li, I. Temprano, C. A. O'Keefe, B. L. Mehdi, M. F. L. D. Volder and C. P. Grey, *ACS Energy Lett.*, 2022, **7**, 3524-3530.
23 T. He, R. Jia, X. Lang, X. Wu and Y. Wang, *J. Electrochem. Soc.*, 2017, **164**, E379.
24 W. Tang, *J. Mater. Chem.*, 2004, **14**, 3457-3461.
25 R. Wang, Y. Wang, C. Xu, J. Sun and L. Gao, *RSC Adv.*, 2013, **3**, 1194-1200.
26 A. Kovtun, D. Jones, S. Dell'Elce, E. Treossi, A. Liscio and V. Palermo, *Carbon*, 2019, **143**, 268-275.
27 F. J. Sonia, H. Kalita, M. Aslam and A. Mukhopadhyay, *Nanoscale*, 2017, **9**, 11303-11317.
28 B. D. Ossonona and D. Bélanger, *RSC Adv.*, 2017, **7**, 27224-27234.
29 Y. C. G. Kwan, G. M. Ng and C. H. A. Huan, *Thin Solid Films*, 2015, **590**, 40-48.
30 M. A. Pimenta, G. Dresselhaus, M. S. Dresselhaus, L. G. Cançado, A. Jorioa and R. Saito, *Phys. Chem. Chem. Phys.*, 2007, **9**, 1276-1290.
31 R. Yuan , Y. Guo , I. Gurgan , N. Siddique , Y.-S. Li , S. Jang , G. A. Noh and S. H. Kim, *Carbon*, 2025, **238**, 120214.
32 K. K. H. D. Silva, P. Viswanath, V. K. Rao, S. Suzuki and M. Yoshimura, *J. Phys. Chem. C*, 2021, **125**, 7791-7798.
33 C. R. Minitha, V. S. Anithaa, V. Subramaniam and R. T. R. Kumar, *ACS Omega*, 2018, **3**, 4105-4112.
34 E. Mahmud and M. R. Islam, *Sci. Rep.*, 2023, **13**, 20967.
35 J. Shen, Y. Hu, M. Shi, X. Lu, C. Qin, C. Li and M. Ye, *Chem. Mat.*, 2009, **21**, 3514-3520.
36 D. C. Marcano, D. V. Kosynkin, J. M. Berlin, A. Sinitskii, Z. Sun, A. Slesarev, L. B. Alemany, W. Lu and J. M. Tour, *ACS Nano*, 2010, **4**, 4806-4814.
37 W. Liu and G. Speranza, *ACS Omega*, 2021, **6**, 6195-6205.
38 Y. Li, J. Liu, X. Wang, X. Zhang, N. Chen, L. Qian, Y. Zhang, X. Wang and Z. Chen, *Small Sci.*, 2023, **3**, 2300045.
39 D. Xiong, X. Li, H. Shan, Y. Zhao, L. Dong, H. Xu, X. Zhang, D. Li and X. Sun, *Electrochim. Acta*, 2015, **174**, 762-769.
40 D. Y. Ko, H. J. Kim, H. Park, E. Kim and H. Kim, ACS Nano, 2025, 19, 16957-16966.
41 Y. Shi, L. Wen, H. Yang, Z. Sun and F. Li, *J. Mater. Chem. A*, 2025, **13**, 36802-36824.
42 N. Zhang, B. Wang, F. Jin, Y. Chen, Y. Jiang, C. Bao, J. Tian, J. Wang, R. Xu, Y. Li, Q. Lv, H. Ren, D. Wang, H. Liu, S. Dou and X. Hong, *Cell Rep. Phys. Sci.*, 2022, **3**, 101197.
43 R. Tatara, P. Karayaylali, Y. Yu, Y. Zhang, L. Giordano, F. Maglia, R. Jung, J. P. Schmidt, I. Lund and S.-H. Y.;, *J. Electrochem. Soc.*, 2019, **166**, A5090.
44 J.-B. Gieu, V. Winkler, C. Courrèges, L. E. Ouatani, C. Tessier and H. Martinez, *J. Mater. Chem. A*, 2017, **5**, 15315-15325.
45 Z. Arthur, H.-C. Chiu, X. Lu, N. Chen, V. Emond, K. Zaghib, D.-T. Jiang and G. P. Demopoulos, *Chem. Commun.*, 2016, **52**, 190-193.
46 Q. Li, Y. Wang, X. Wang, X. Sun, J.-N. Zhang, X. Yu and H. Li, *ACS Appl. Mater. Interfaces*, 2019, **12**, 2319-2326.
47 A. Jarry, S. Gottis, Y.-S. Yu, J. Roque-Rosell, C. Kim, J. Cabana, J. Kerr and R. Kostecki, *J. Am. Chem. Soc.*, 2015, **137**, 3533-3539.
48 L. Wheatcroft, T. D. Tran, D. Özkaya, J. Cookson and B. J. Inkson, *ACS Appl. Energy Mater.*, 2022, **5**, 196-206.
49 J. L. Tebbe, A. M. Holder and C. B. Musgrave, *ACS Appl. Mater. Interfaces*, 2015, **7**, 24265-24278.
50 Y. Ma, Y. Zhou, C. Du, P. Zuo, X. Cheng, L. Han, D. Nordlund, Y. Gao, G. Yin, H. L. Xin, M. M. Doeff, F. Lin and G. Chen, *Chem. Mat.*, 2017, **29**, 2141-2149.
51 S. Wolf, M. Roschger, B. Genorio, D. Garstenauer and V. Hacker, *ACS Omega*, 2023, **8**, 11536-11543.
52 P. V. Kamat, *J. Phys. Chem. Lett.*, 2009, **1**, 520-527.
53 L. Liu, X. Zhao, G. Ding, C. Han and J. Liu, *Chem. Eng. J.*, 2023, **470**, 143820.
54 J. L. Allen, T. R. Jow and J. Wolfenstine, *J. Power Sources*, 2011, **196**, 8656-8661.
55 E. Markevich, R. Sharabi, H. Gottlieb, V. Borgel, K. Fridman, G. Salitra, D. Aurbach, G. Semrau, M. A. Schmidt, N. Schall and C. Bruenig, *Electrochem. Commun.*, 2012, **15**, 22-25.
56 Q. D. Truong, M. K. Devaraju, T. Tomai and I. Honma, *ACS Appl. Mater. Interfaces*, 2013, **5**, 9926-9932.
57 E. Markevich, G. Salitra, K. Fridman, R. Sharabi, G. Gershinsky, A. Garsuch, G. Semrau, M. A. Schmidt and D. Aurbach, *Langmuir*, 2014, **30**, 7414-7424.
58 Y. H. Ikuhara, X. Gao, C. A. J. Fisher, A. Kuwabara, H. Moriwake, K. Kohama, H. Iba and Y. Ikuhara, *J. Mater. Chem. A*, 2017, **5**, 9329-9338.
59 M. G. Palmer, J. T. Frith, A. L. Hector, A. W. Lodge, J. R. Owen, C. Nicklinb and J. Rawle, *Chem. Commun.*, 2016, **52**, 14169-14172.

View Article Online
DOI: 10.1039/D6EB00077K

60 J. L. Allen, J. L. Allen, T. Thompson, S. A. Delp, J. Wolfenstine and T. R. Jow, *J. Power Sources*, 2016, **327**, 229-234.
61 F. C. Strobridge, R. J. Clément, M. Leskes, D. S. Middlemiss, O. J. Borkiewicz, K. M. Wiaderek, K. W. Chapman, P. J. Chupas and C. P. Grey, *Chem. Mater.*, 2014, **26**, 6193-6205.
62 S. Sreedeep, S. Natarajan and V. Aravindan, *Curr. Opin. Electrochem.*, 2022, **31**, 100868.
63 W. M. Dose, I. Temprano, J. P. Allen, E. Björklund, C. A. O'Keefe, W. Li, B. L. Mehdi, R. S. Weatherup, M. F. L. D. Volder and C. P. Grey, *ACS Appl. Mater. Interfaces*, 2022, **14**, 13206-13222.
64 M. Gauthier, T. J. Carney, A. Grimaud, L. Giordano, N. Pour, H.-H. Chang, D. P. Fenning, S. F. Lux, O. Paschos, C. Bauer, F. Maglia, S. Lupart, P. Lamp and Y. Shao-Horn, *J. Phys. Chem. Lett.*, 2015, **6**, 4653-4672.

View Article Online
DOI: 10.1039/D6EB00077K

Data availability

The data that supports the findings of this study have been included as part of the supplementary information (SI). SI is available. See DOI: http://. Further information is available from the corresponding author upon reasonable request